Multi-Watt-Level 4.9-GHz Silicon Power Amplifier for Portable Thermoacoustic Imaging

Christopher Sutardja, *Member, IEEE*, Ajay Singhvi, *Graduate Student Member, IEEE*, Aidan Fitzpatrick, *Graduate Student Member, IEEE*, Andreia Cathelin, *Senior Member, IEEE*, and Amin Arbabian, *Senior Member, IEEE*

***Abstract*— Microwave-induced thermoacoustic (TA) imaging, combining high microwave contrast with high ultrasonic resolution has the potential to revolutionize applications such as continuous healthcare monitoring, point-of-care imaging, and biometric authentication. However, the size, cost, and integration of a high-power microwave transmitter is a key bottleneck in making TA imaging truly portable, affordable, and ubiquitous. Toward that end, this work presents a compact 4.9-GHz pulsed power amplifier (PA) with a 4.87-mm^2 active area implemented in a 55-nm BiCMOS technology, operating in a duty-cycled mode and achieving 37.3-dBm peak output power—the highest demonstrated peak power in PAs fabricated on a silicon substrate with deep submicron CMOS integration. We also reconstruct the first known high-fidelity TA images of tissue phantoms using an integrated silicon PA.**

***Index Terms*— BiCMOS, biomedical imaging, HBT, high power, power amplifier (PA), thermoacoustic (TA) imaging, ultrasound.**

I. Introduction

HANDHELD and portable medical imaging systems have the potential to make a disruptive impact across a number of application spaces. Wearable devices which continuously monitor specific health parameters for early intervention and disease management are becoming increasingly ubiquitous as they offer a promising avenue for automated, personalized health care [1]. Point-of-care ultrasound [2] and microwave imaging [3] systems have enabled long-term, at-home monitoring, as well as increased access to quality healthcare in communities that have poor traditional healthcare infrastructure. Additionally, sophisticated optical and ultrasound systems leveraging medical imaging technologies have also been deployed in smartphones and elsewhere for convenient biometric authentication via fingerprint readers and face scanners [4].

Manuscript received September 19, 2021; revised November 29, 2021 and January 26, 2022; accepted January 27, 2022. This article was approved by Associate Editor Domine Leenaerts. This work was supported in part by the National Institutes of Health (NIH) R21 under Grant R21AI163489 and in part by the Stanford System-X Alliance. *(Corresponding author: Christopher Sutardja.)*

Christopher Sutardja, Ajay Singhvi, Aidan Fitzpatrick, and Amin Arbabian are with the Department of Electrical Engineering, Stanford University, Stanford, CA 94305 USA (e-mail: sutardja@stanford.edu; asinghvi@stanford.edu; ajfitz@stanford.edu; arbabian@stanford.edu).

Andreia Cathelin is with the Technology Research and Development Department, STMicroelectronics, 38926 Crolles, France (e-mail: andreia.cathelin@st.com).

Color versions of one or more figures in this article are available at https://doi.org/10.1109/JSSC.2022.3149910.

Digital Object Identifier 10.1109/JSSC.2022.3149910

Despite these inroads, most technologies deployed in such portable devices today have a few significant shortcomings. Optical imaging techniques often only image surface-level features with sufficient fidelity [5]. Microwave imaging devices leverage the high dielectric contrast in tissue but are hamstrung by the tradeoff between penetration depth and image resolution tied to the microwave operation frequency [6]. Ultrasound imaging offers high resolution due to the smaller acoustic wavelength, but suffers from poor mechanical contrast in soft tissue [7]. A technology that overcomes these limitations would not only improve the capabilities of existing portable imaging solutions, but could also open the door to completely new application spaces.

Microwave-induced thermoacoustics (TAs)—a hybrid, multiphysics imaging modality—overcomes these limitations by decoupling the excitation and detection mechanisms to offer the best of both worlds: high dielectric contrast via microwave excitation and good resolution through ultrasonic detection. TA imaging has shown impressive results for blood vessel imaging [5], breast cancer screening [8], and thermometry [9], among other applications. In the push to make TA imaging systems more compact, the detection subsystem can be implemented using miniaturized ultrasound sensor-on-chip architectures already demonstrated in literature [10]–[12]. However, miniaturizing the excitation subsystem poses a greater challenge—most TA imaging demonstrations to-date utilize bulky, high-power vacuum sources or benchtop III–V semiconductor microwave power sources [13] for exciting the TA signal, ultimately restricting current TA imaging systems to research or lab-based settings.

To overcome this bottleneck in the TA transmitter and achieve the holy grail of a portable and low-cost multimodal imaging system, this article focuses on the design of a millimeter-sized, high-power, integrated microwave power amplifier (PA). Such a PA could enable targeted TA excitation of blood vessels or other water-dense tissue as conceptually illustrated in Fig. 1. This could be achieved with a single-chip configuration through proximity of the microwave applicator to regions of interest or through a multi-chip configuration which leverages beamforming techniques.

As depicted in Fig. 1(b), an array of compact PA ICs could enable spatial power combining at a targeted depth in tissue to increase the microwave power deposited without being limited by the peak power per chip. The concept of TA beamforming was first demonstrated in [8] in which four microwave transmitters each with output power P_{out}

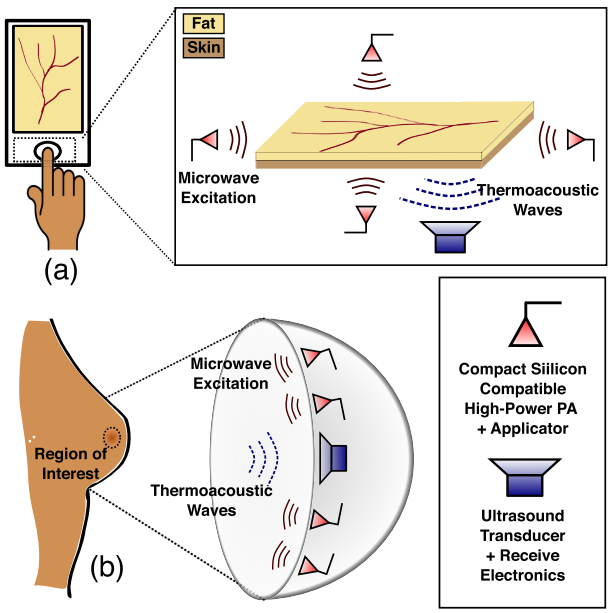

Fig. 1. Conceptual illustration of an integrated TA imaging system for (a) blood vessel imaging and (b) breast cancer screening using compact, high-power silicon PA ICs as TA transmitters.

provided increased SNR in comparison to a single microwave transmitter with output power $4 \times P_{\text{out}}$. The SNR gain provided by spatial power combining would continue to scale with the number of microwave transmitters, yet larger arrays have not been demonstrated due to the lack of compact, high-power microwave PA ICs.

PAs fabricated on a silicon substrate with deep submicron CMOS integration would permit a densely integrated TA imaging system—encompassing components of the ultrasound detection and microwave excitation subsystems as well as any peripheral circuitry and digital signal processing units. Previous works on high-power integrated PAs were fabricated in processes without CMOS integration [14], so peripheral circuitry could not be easily integrated. Recent works on high-power silicon CMOS PAs focus on efficiently achieving continuous-wave, watt-level output power at mm-wave frequencies for 5G communication systems [15], [16]. In contrast, we aim to develop a pulsed PA operating at 4.9 GHz that pushes the limits of the maximum peak power achievable in a silicon substrate with deep submicron CMOS capability to facilitate high-SNR and high-resolution TA imaging as first introduced in [17].

A 37.3-dBm peak-power pulsed PA with 42% collector efficiency and pulsewidth modulation ranging from 50 ns to 2 μs is demonstrated in a 55-nm BiCMOS SiGe process, using four stacked current-mode Class-D unit cells connected to distributed active transformers (DATs). Driver stages constructed using current-mode logic (CML) inverters mitigate the increased risk of oscillations in the design of a high-power PA by lowering the gain of any parasitic feedback loops which could cause instability. In addition, pulse control is implemented through current-starved inverters to ensure reliable operation of the PA by controlling the rise times of any fast transients that could lead to device breakdown. The proposed PA IC has the highest published peak output power in a multi-GHz PA built on a silicon substrate with deep submicron CMOS integration. The article also shows, for the first time, end-to-end experimental TA imaging results using an integrated silicon PA as the microwave transmitter. This PA, which covers an area of only 4.87 mm^2, could be integrated to create a portable TA imaging system with radically scaled-down system size. In addition, the design insights presented throughout are also applicable to high-power PA design across a variety of applications.

This work extends [17] to include detailed analysis, design challenges, methodology, and simulations for the high-power PA as well as new experimental TA imaging results using a multi-chip excitation scheme. The article is organized as follows: Section II discusses the basic principles of the TA effect and their implication on the PA design as well as choices of the technology node and high-power PA design techniques. Section III provides details about the chosen PA architecture, circuit-level challenges, schematics, and simulations. Section IV presents comprehensive chip measurement results and comparison with the state-of-the-art. Finally, Section V includes results of TA sensing and imaging experiments with the PA IC(s) as the TA transmitters.

II. High-Power PA for TA Imaging

A. Design Goals and Challenges

Whereas the design of PAs for wireless transmitters balances efficiency, linearity, and power over continuous wave outputs, microwave transmitters in TA imaging systems have a different design space over which we aim to optimize.

Microwave TA imaging systems typically operate in a pulsed excitation configuration such that a modulated pulse of microwave energy is coupled to a target and an ultrasonic pulse is generated through the TA effect. The characteristics of the ultrasonic pulse, or TA signal, are dependent on the microwave carrier frequency, pulsewidth, and peak power and are governed by the TA wave equation [5]

$$\left(\nabla^2 - \frac{1}{v_s^2}\frac{\partial^2}{\partial t^2}\right) p(r,t) = -\frac{\beta}{C}\frac{\partial Q(r,t)}{\partial t} \tag{1}$$

where the acoustic pressure $p(r,t)$ is proportional to the absorbed microwave energy $Q(r,t)$

$$Q(r,t) \approx \left[\sigma(f) + 2\pi f \cdot \epsilon''(f)\right] \cdot |E(r,t)|^2. \tag{2}$$

As can be noted in (2), the conductivity σ and the complex permittivity ϵ'' determine the amount of microwave power ($\propto |E(r,t)|^2$) absorbed by the tissue—both of which are highly dependent on the microwave frequency f. Therefore, to maximize the SNR of the TA imaging system, it is critical to prioritize the peak output power of the PA and to select an appropriate microwave frequency. Prior works have shown that a 5-GHz microwave frequency is a near ideal operating condition for a variety of TA imaging applications [5], [8], [18].

Whereas the microwave carrier frequency impacts the degree of tissue absorption, the envelope of the microwave excitation dictates the acoustic frequency spectrum of the

generated TA signal [19]. Similar to ultrasound imaging, the selection of the TA signal's frequency can also impact system SNR considerably due to the frequency-dependent acoustic attenuation in tissue [7]. Typical diagnostic medical ultrasound imaging operates in the regime of 1–10 MHz depending on the application. To have the provisions to cover the same acoustic frequency range, our PA must be capable of transmitting a pulse or train of pulses with pulse widths between 50 and 500 ns [19]. Like in pulse-echo ultrasound imaging [7], the pulse repetition frequency or duty cycle of the microwave excitation determines the maximum unambiguous imaging depth and frame rate of TA imaging. Within the above acoustic frequency range, a duty-cycle of 1% offers a reasonable balance between imaging frame rate and maximum imaging depth.

With these desired specifications in mind, we aim to design an mm-sized, high peak-power PA operating at 5 GHz with capability to output pulse widths as low as 50 ns.

B. Technology Node

While III–V processes like GaN and GaAs have great RF performance, integration challenges preclude their usage for an application that requires a compact form factor. That said, generating high output power using purely CMOS processes at our frequencies of interest is limited by either low break-down voltages or low device f_T [20], [21].

BiCMOS SiGe technologies offer high-power, RF performance while also allowing for close integration. Thus, we choose a 55-nm BiCMOS process which provides high-speed SiGe HBTs that have much higher f_T along with high-voltage SiGe HBTs with higher breakdown voltage than CMOS devices in comparable technologies [22], while still having the option to use submicron CMOS devices for easier integration with peripheral analog and digital circuitry.

C. High-Power RF PA Design Techniques

Scaling of CMOS processes has brought increased device speeds and enabled higher levels of integration but as a result, the breakdown voltages of transistors have reduced, which limits the achievable output power. Series stacking of transistors has been proposed for RF PAs to mitigate the effects of lower breakdown voltage from deep submicron scaling. If only one type of transistor is available, then it is ideal to equally spread the collector voltage across each transistor in the stack [23].

The high-voltage HBTs available in the 55-nm BiCMOS process make a hybrid stacking approach possible, as shown in Fig. 2. In this configuration, we use the high-speed HBT as the input device because it has high current gain while the majority of the voltage drop occurs across the high-voltage HBT employed as the cascode device. Other works have shown that under the proper base impedance termination and collector current density, the collector breakdown voltage of the high-voltage HBT exceeds $\mathrm{BV_{CEO}}$ and approaches the much higher value $\mathrm{BV_{CBO}}$ [24], allowing us to greatly increase the output power of an HBT PA in a BiCMOS process. This impedance termination is implemented as shown in Fig. 2,

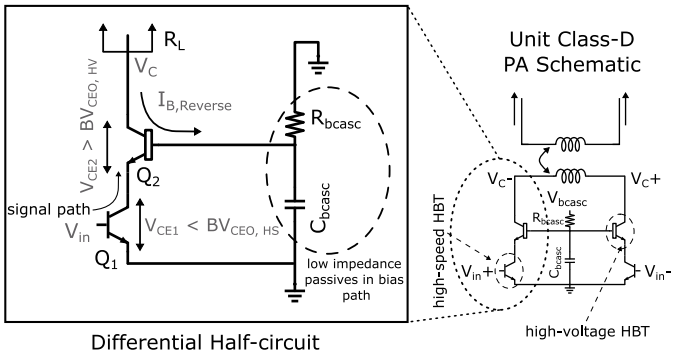

Fig. 2. Hybrid stacking approach with high-speed and high-voltage HBTs. Majority of voltage drop is across the high-voltage HBT. R_{bcasc} and C_{bcasc} absorb reverse base current from Q_2 without slowing circuit operation.

by connecting the base to a low-impedance path by using a large common-mode capacitor (C_{bcasc}) and a low base resistance (R_{bcasc}). C_{bcasc} absorbs any transient excess charge from base-current reversal to ensure we do not exceed collector current density limits. It is important to note that these low impedances are not in the signal path of the PA, so they do not slow down PA operation.

Transformer-based power combining is a commonly used method for increasing PA output power [21], [25]. Outputs of multiple unit amplifiers can be combined by connecting the secondary turns of their output transformers in series or in parallel. A high number of stages combined using a series transformer connection results in a high load impedance for the PA, while multiple parallel transformer connections result in a low-load impedance. Combining using both series and parallel configurations can lead to a load impedance closer to the 50-Ω characteristic impedance of many transmission lines that interface with the chip. The efficiency of higher-order power-combining schemes is limited by the increased parasitics of larger passive combiner networks. As the number of on-chip power combining networks increase, we face diminishing returns in both area and power efficiency [21], [25]. Thus, we choose to design a PA with a 2×2 power combining configuration, where two series-combined DATs are placed in parallel with each other. Spatial power combining using multiple chips provides us with another alternative to increase effective isotropic radiated power (EIRP) for TA imaging [8].

We utilize a combination of these high-power design techniques in our final PA architecture as illustrated in Fig. 3 with further implementation details discussed in Section III.

D. PA Class

The choice of PA class offers a tradeoff between efficiency, linearity, and output power. Class-A PAs offer excellent linearity and high peak power, but suffer from poor efficiency, while Class-E PAs sacrifice linearity to achieve high efficiencies which reduces power in the fundamental frequency. While Class-F PAs have been used for efficient PA designs, the quarter-wave transmission lines or multiple parallel *LC* tanks that are used for harmonic isolation would be prohibitively large to design at our frequencies of interest. We thus choose

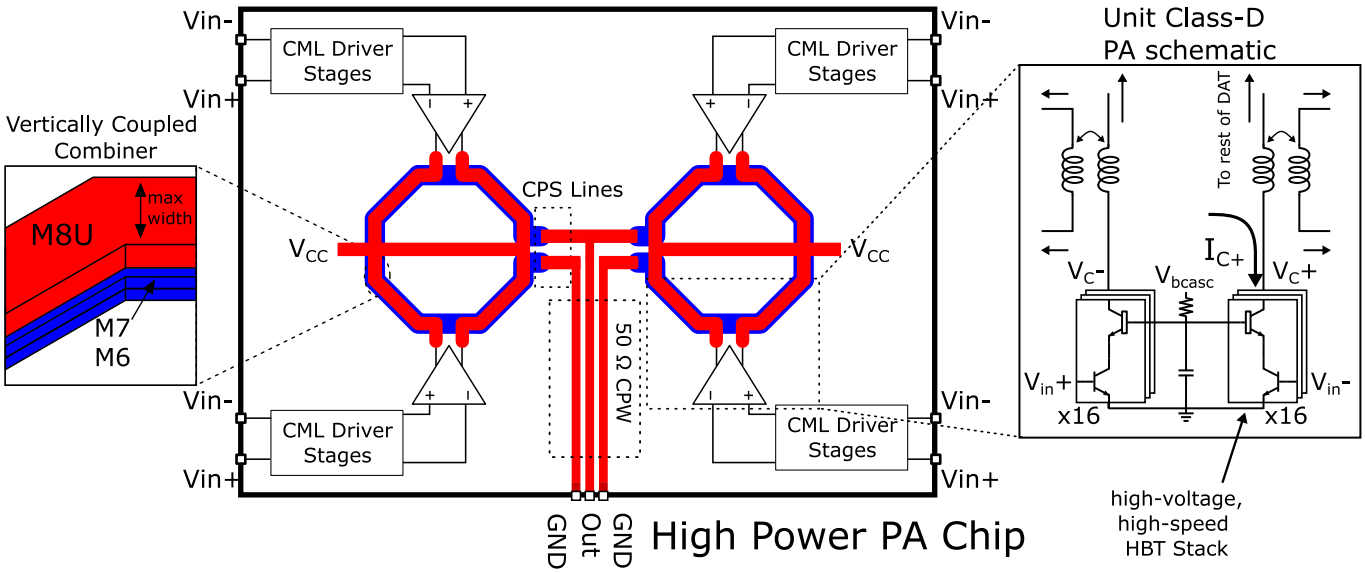

Fig. 3. Overall architecture of the proposed high-power PA chip which uses CML inverters to drive four stacked Class-D PA unit cells that are combined using a 2 × 2 DAT to generate a multi-watt level output.

to go with a current-mode Class-D PA as it has a higher output power at the fundamental frequency than most other switching PAs, while being reasonably efficient [26].

For differential current-mode Class-D operation [27], an ideal unit PA will have an output power of

$$P_{\text{unit}} = \frac{2V_{\text{CC}}^2}{\pi R_L} \tag{3}$$

where V_{CC} is the power supply of the PA, and R_L is the load resistance. When using a 2 × 2 power transformer combining scheme as discussed above, the output power can be approximated as

$$P_{\text{out}} = 4P_{\text{unit}}\eta \tag{4}$$

where η is a combined metric that incorporates the efficiency and coupling of the transformer combiner. A Class-D PA connected to its supply through an inductive choke would have a peak-to-peak output amplitude of around double the supply voltage. To prevent the voltage on the device from going above BV_{CBO} of the high-voltage HBT of the 55-nm process, we assume safe PA operation at a V_{CC} of 7 V. For a 7-V V_{CC}, an R_L of 50 Ω, and η of 0.7, the first-order output power of such an architecture approaches 7 W—which would be the highest demonstrated peak power in a PA fabricated on a silicon substrate with submicron CMOS integration.

III. Circuit Implementation

A. PA Architecture

Fig. 3 shows the block diagram of the proposed high-power PA. Each differential Class-D PA unit cell consists of a high-speed HBT stacked with a high-voltage HBT. The cascode high-voltage HBT operates in a "beyond BV_{CEO}" regime to maximize collector voltage swing. To aid in device stability, the collector voltage of the high-speed HBT input device does not exceed BV_{CEO} to prevent base current reversal. The

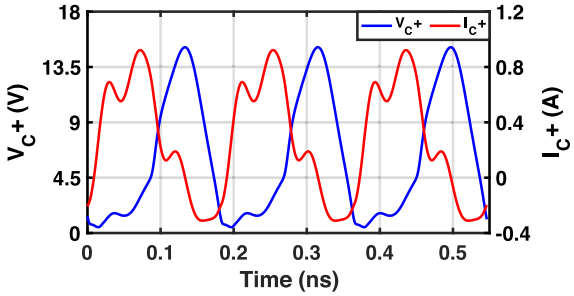

Fig. 4. Simulated transient waveforms of the output stage of a unit PA. Note that current waveforms include both transistor currents and collector capacitor currents.

differential Class-D unit cells are implemented by connecting 16 maximum-sized HBTs in parallel and laid out in an H-tree configuration to minimize the imbalance of routing parasitics. Fig. 4 shows the extracted transient simulation current and voltage waveforms for the Class-D unit cell.

Four PA unit cells are connected through series–parallel transformer-based power combining in a 2 × 2 configuration as seen in Fig. 3. Each combiner consists of two unit PA stages with their output voltages combined by connecting their secondary coils in series. The output currents of the two combiners are then summed by connecting them in parallel through coplanar striplines (CPSs) joined into a single coplanar waveguide (CPW) to send the signal off-chip. The primary and secondary coils of each combiner are vertically coupled to increase the coupling factor [28]. To prevent excessive electromigration and to maximize dc current carrying ability, the primary coils of the power combiners are constructed on the ultra-thick top metal layer (M8) with a maximum width, 25 μm copper traces, whereas the secondary coils are constructed on a M6–M7 layer stack.

Reaching multi-watt-level output power requires the PA to have multiple driver stages to gain up the input signal to the

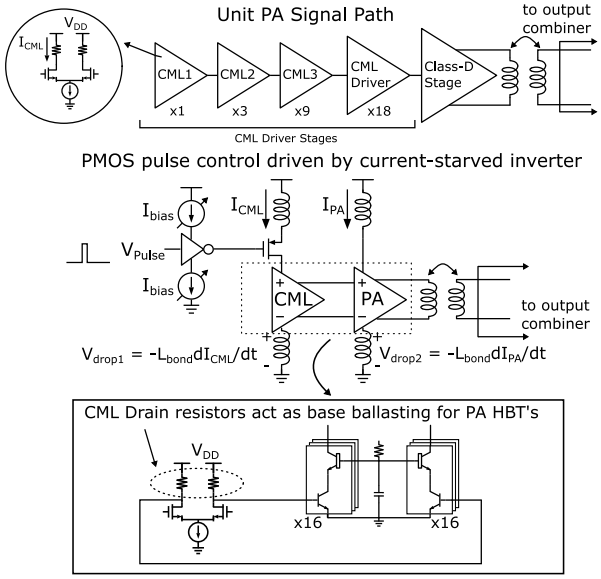

Fig. 5. Top-level diagram of unit PA stage, CML driver schematic, pulse rise time control mechanism, and base ballasting from the pull-up resistors of CML driver.

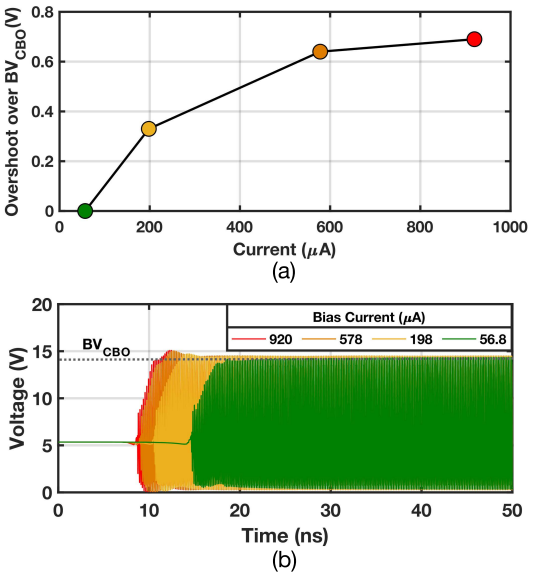

Fig. 6. Simulations showing (a) voltage overshoot over BV_{CBO} and (b) voltage drop on PA HBTs if inverter bias currents are too high.

appropriate level. If all these driver stages were implemented as conventional RF amplifiers with tuned LC loads, each stage would require a large inductor or power combiner. Instead, the driver stages are implemented as resistively loaded CML inverters to save area as well as to maintain stability as discussed further in Section III-B. Fig. 5 shows four CML stages which are cascaded to drive the PA unit cell.

Operation of the PA for narrow pulse widths creates unique challenges due to fast rise times. When the PA output turns on, the current consumption rapidly goes from near zero to over 3 A. The rise time of the pulse envelope of the PA must be sufficiently managed because high dI/dt voltage drops across bondwire inductances could potentially damage on-chip devices. As shown in Fig. 5, a pMOS header device on top of the CML driver is used to pulse the voltage supply of the output stage for each PA unit cell to achieve the desired pulse modulation. The pMOS header device is driven by a current-starved inverter to control the rise time of the current waveform. The inverter is biased using a current mirror referenced to a programmable external resistor. Proper choice of this bias current is critical to avoid the possibility of HBT breakdown. Fig. 6 shows the transient voltage across the collector and emitter of the high-voltage cascode HBTs used in the unit PAs. If the bias current is too high, the V_{CE} of the cascode device can have voltage transients that exceed the BV_{CBO} of the transistor, greatly increasing risk of device damage over time.

Thermal runaway is another common challenge when operating HBT devices at high current levels and can lead to overheating ICs [26]. To mitigate any such issues, we implement base ballasting with added resistors as shown in Fig. 5, though the duty-cycled operation for our imaging application also lowers the possibility of thermal runaway.

Thus, our choices for the PA input driver stages, PA unit cell, and output power combining all play a key role in the design of an area-efficient, high-power PA that has safeguards against device breakdown and instability.

B. PA Stability

Instability is a primary threat to proper PA operation at high P_{sat} levels. The large C_μ and high gain of the HBT input device can result in PA input impedance with a negative real part, potentially causing oscillations at unwanted frequencies and limiting peak output power. We alleviate the possibility of differential mode (DM) oscillations by employing capacitive neutralization to reduce differential collector-base feedback capacitance, though this increases the equivalent C_μ in common mode (CM) operation and is thus insufficient to prevent instability on its own.

To prevent such instability, we drive the HBTs of the PA cell using CML inverters with a carefully chosen pull-up drain resistance. Fig. 7 shows the DM and CM equivalent half-circuits at the interface between the final CML driver stage and the PA cell prior to capacitive neutralization. The impedance looking into this node is denoted as Z_{total}—if the real part of Z_{total} is negative, there is a high chance of oscillation at undesired frequencies. In DM operation, low R_D creates a low resistance path in parallel with any potential negative input impedance looking into the HBT, which now ensures Z_{total} has a positive real part. In CM operation, R_D is in series with the bondwire inductance, de-Qing any potential LC network in the feedback path—with increased de-Qing for larger values of R_D. Also, compared to a linear PA, the overall CM gain of a differential switching PA is lower because one side of the PA is off at all times.

Fig. 8 shows the simulated peak power versus CML load resistance, R_D. As R_D falls, the Q of the common-mode feedback networks increases, so the likelihood of oscillation also increases. Common-mode oscillation can create an unwanted envelope modulation on the output signal of the PA, lowering

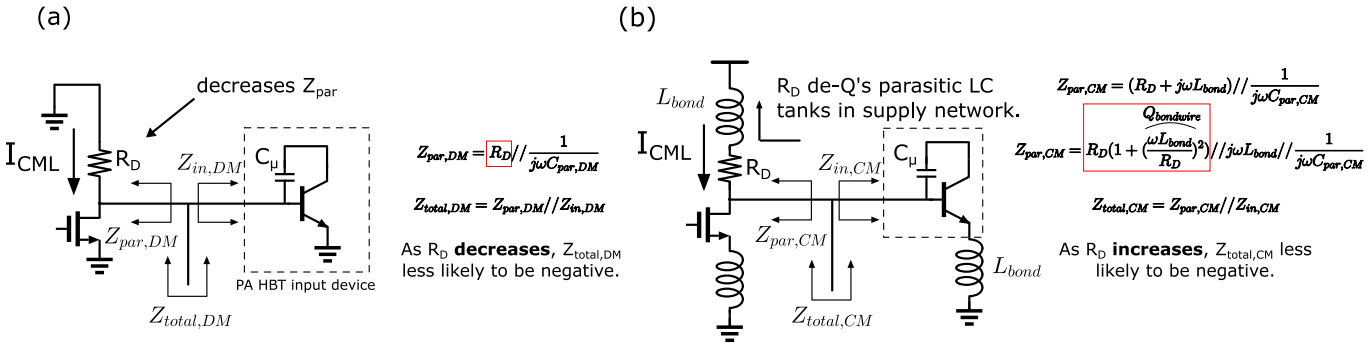

Fig. 7. Differential-mode and common-mode half-circuit diagrams showing the impedances of the node at the input of the PA unit cell prior to capacitive neutralization. There is a risk of oscillation if the pull-up resistor, R_D, of the CML is either too small or too large. (a) Differential-mode half-circuit. (b) Common-mode half-circuit.

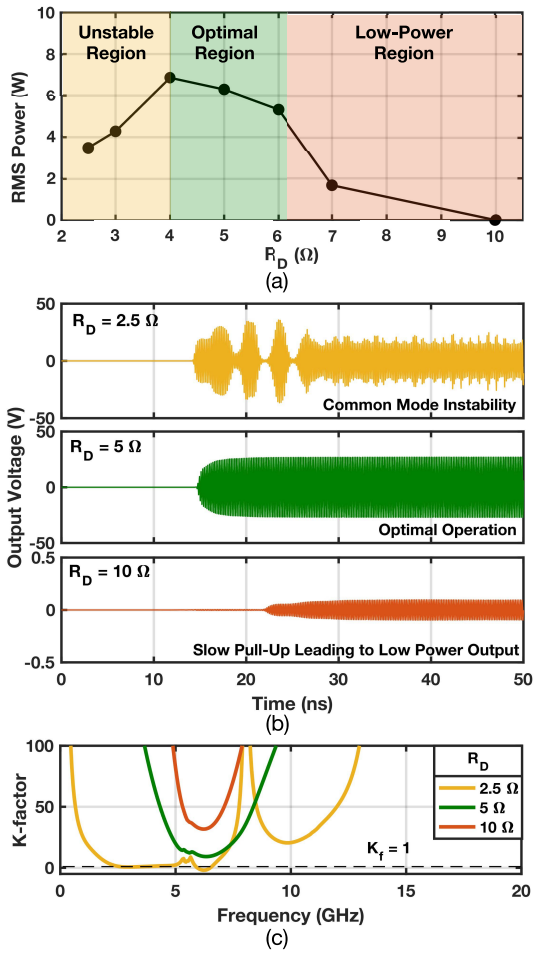

Fig. 8. (a) Simulated PA output power versus R_D of CML driver. (b) Transient output waveforms at various R_D—at low R_D, PA output suffers CM instability, and at large R_D, lower output power due to slow pull-up from the driver. (c) Rollet's K-factor simulations demonstrating PA stability for various R_D values.

the rms output power. At large values of R_D, output power falls due to slower charging of the input capacitor of the PA unit cell. Rollet's K-factor simulations are also shown in Fig. 8 to demonstrate the effect that R_D has on the stability of the PA. The stability simulations are done using Periodic S-Parameter (PSP) simulations in Spectre that are linearized around a chosen dc operating point, so the full nonlinear

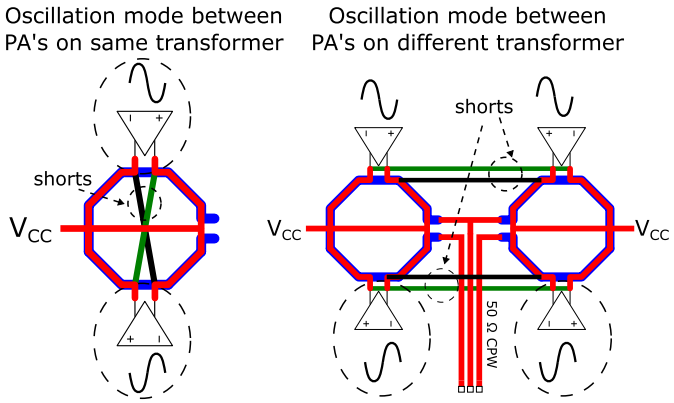

Fig. 9. Higher-order modes of oscillation in a power-combined PA. Oscillation between two unit PAs can be suppressed by shorting nodes of equal polarity.

gain of the HBT PA device is not fully captured. Although $K_f > 1$ is a promising sign of stability, large signal transient sims are required to confirm stability. Thus, there is an optimal range of R_D values that ensures stable operation in both CM and DM while retaining high power output. For this design, an R_D of 5 Ω was chosen as the pull-up resistor value for the CML driver stage.

Higher-order instability can also cause concern. Even if CM and DM oscillations are suppressed in each unit PA, one unit cell could oscillate relative to another PA cell. Fig. 9 shows the various modes of oscillations that can occur. We avoid such instability by shorting nodes of equal polarity as it decreases the impedance, in turn reducing the differential gain between two nodes prone to oscillation. Such shorts between nodes of the same polarity are implemented within the same combiner, as well as across the two combiners [29].

IV. Electrical Measurements

The PA is fabricated in a 55-nm SiGe BiCMOS process and occupies an area of 2660 × 1829 μm^2, as shown in the die photo in Fig. 10. For improved heat sinking capabilities, the chip is wire-bonded onto an Isola Astra MT77 PCB. Fig. 10 shows the two configurations for the measurement setup of the PA: large signal power measurements and pulse envelope characterization. Due to the high power nature of the PA,

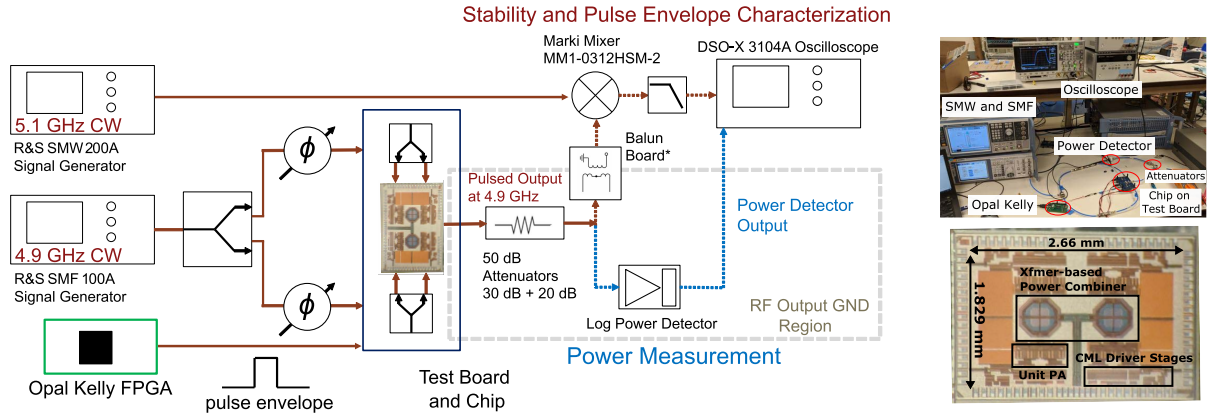

Fig. 10. Schematic showing electrical measurement setup, lab-based photograph of electrical measurement setup, and die photograph.

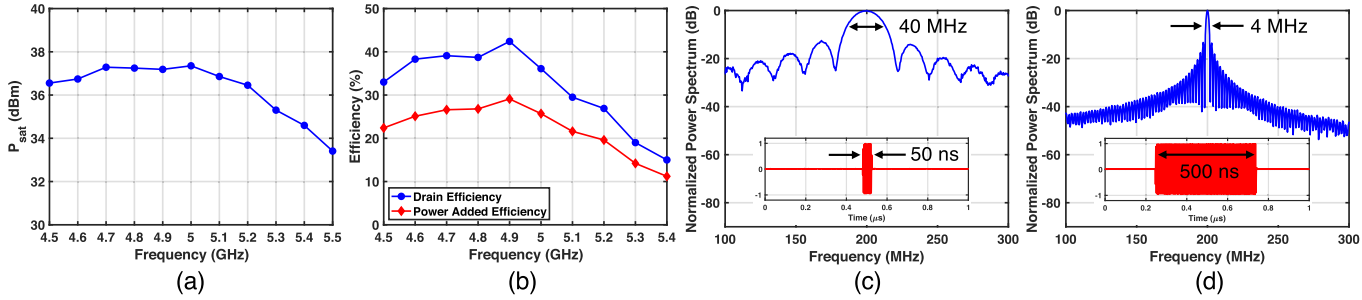

Fig. 11. (a) Peak output power versus frequency, (b) collector efficiency and PAE versus frequency, (c) PA time domain and IF spectrum measurements of a 50-ns pulse, and (d) PA time domain and IF spectrum measurements of a 500-ns pulse.

the output must be connected through fixed attenuators to the measurement equipment.

Output power measurements are conducted by connecting the chip output through 50 dB of fixed attenuators before measuring the total power of the envelope through a logarithmic power detector. Because the PA is designed to operate in a duty-cycled mode, pulsed measurements are taken at varying pulse widths. Fig. 11(a) and (b) shows P_{sat}, collector efficiency, and PAE measured over various carrier frequencies. For pulse widths ranging from 50 ns to 2 μs, the PA achieved 37.3 dBm peak P_{sat} with 42% collector efficiency at 4.9 GHz.

By mixing the 4.9-GHz PA output with a 5.1-GHz reference signal, we downconvert the output to a 200-MHz IF to visualize the instantaneous bandwidth and stability of the PA. Fig. 11(c) and (d) shows the normalized power spectrum of 50 and 500 ns pulses, respectively. One sign of instability is an unwanted envelope modulation of the PA output, which manifests as large spurs in the power spectrum. As the spectrum measurements show, there are no detectable spurs near the frequencies of interest indicating stable PA operation.

Reliability measurements are done to show that the PA can operate over long periods of time without performance degradation or thermal runaway. Fig. 12 shows measured peak power and die temperature versus time for two separate PA boards. The temperature measurements are conducted using an infrared thermometer focused on the surface of the bare die. The pulsewidth of the PA is set at 1.5 μs and the duty cycle is set at 150 μs to mimic the stated operating conditions of a 1% duty cycle for the PA. A typical measurement of subcutaneous vasculature for biometric authentication would take less than a minute [5]. So, the measurement shows reliability over a time that is 10–100× greater than would be used in a practical imaging system.

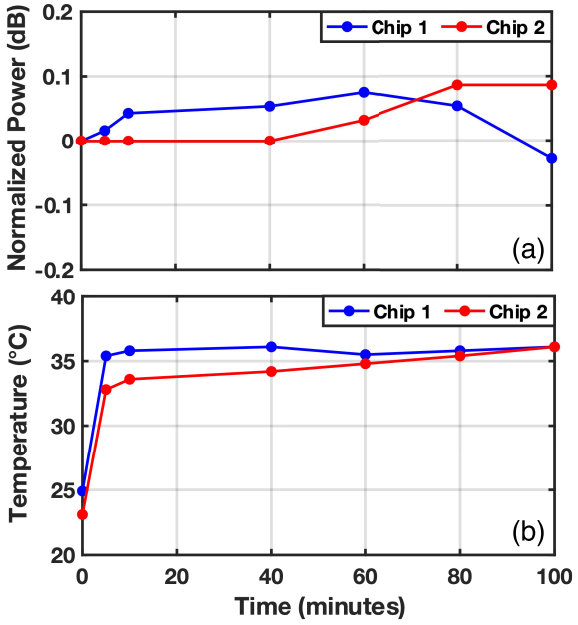

Fig. 12. (a) Normalized peak output power and (b) temperature measurements for two chips over 100 min of 1% duty-cycle PA operation. Thermal runaway does not occur.

TABLE I
PERFORMANCE COMPARISON WITH STATE-OF-THE-ART PAS

	Microwave PAs					mm-wave PAs	
	This work	Aoki [20]	Fathi [21]	Ju [30]	Serhan [31]	Datta [15]	Nguyen [16]
Architecture	Stacked Class-D^{-1} DAT	Concentric DAT	2 × 2 xformer combining	Linear Class-AB	Doherty	Stacked Class-B	Asymmetric DAT
Frequency (GHz)	4.9	0.9	5.3	5.0	2.3	46	60
Supply (V)	6.85	3.5	6.35	5	5	5	2.2
Gain (dB)	26	N/A	16.9	31.8	27.9	13	24.7
Peak P_{sat} (dBm) (V)	37.3	35	30.3	33	35.8	28.9	30.1
Collector/Drain Efficiency (%)	42.4	N/A	19.4	N/A	N/A	N/A	N/A
Peak PAE (%)	29.1	51	18.2	35.5	57	18.4	20.8
Modulation	Pulsed UWB	EGSM-900	Single-Tone CW	802.11ac/ax	LTE QPSK	N/A	16-QAM
Operation Mode	Duty-Cycled	Continuous-Wave	Continuous-Wave	Continuous-Wave	Continuous-Wave	Continuous-Wave	Continuous-Wave
Active Area (mm^2)	4.87	4.2	5.88	2.03	2.21	13.7	6.6
Technology	55 nm BiCMOS	0.13 μm CMOS	65 nm CMOS	0.35 μm SiGe	130 nm CMOS SOI	0.13 μm SiGe	45 nm CMOS SOI

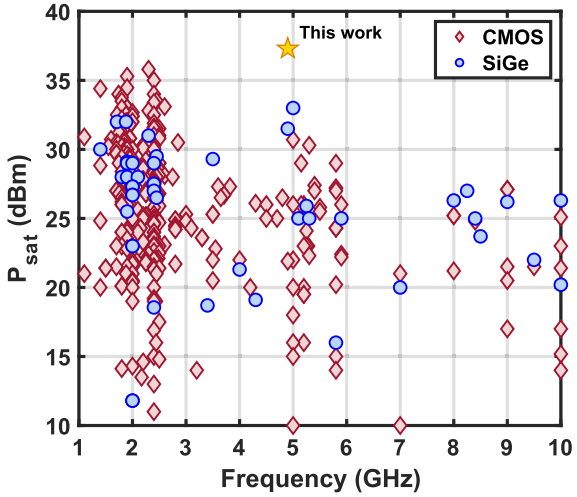

Fig. 13. Peak P_{sat} comparison with other high power CMOS and SiGe PAs at frequencies of interest.

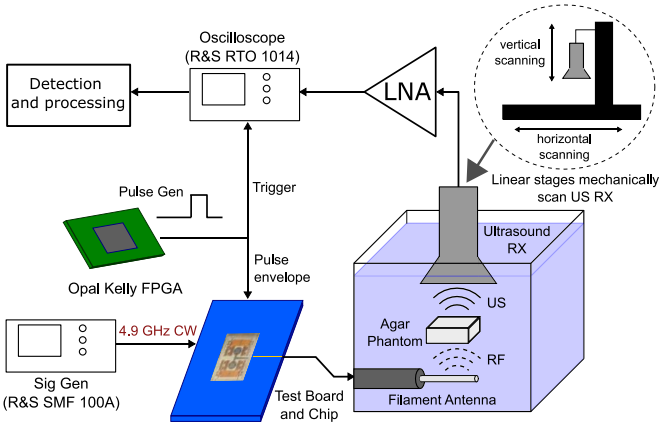

Fig. 14. Experimental setup of the TA imaging system.

In Table I, performance metrics are compared across state-of-the-art high-power PAs. Of over 1000 CMOS and SiGe PAs collected in [32], a selection of which are shown in Fig. 13, the proposed PA has the highest demonstrated peak output power at multi-GHz frequencies, while still achieving competitive collector efficiency and PAE.

V. EXPERIMENTAL TA IMAGING

A. Experimental Setup

Targeted TA excitation, whether achieved through proximity of an antenna or through power combining beamforming techniques, could be enabled by mm-sized silicon PAs. To demonstrate this concept, we present ex-vivo TA imaging results using the presented PA.

In the experiments, blocks of agarose gel act as phantoms which mimic the RF absorption properties of blood vessels or water-dense tissue [33]. As seen in Fig. 14, these phantoms are immersed in mineral oil that has similar acoustic properties to that of human tissue [5].

Serving as a microwave transmitter, the designed PA and test board feeds a customized monopole filament antenna that couples the microwave power to the agarose phantoms. To capture the generated TA signals, a commercial ultrasound transducer (Olympus A303S) is submerged in the oil. The transducer has a 1-MHz center frequency and a quality factor (Q) of 3. Therefore, to ensure efficient detection of the TA signals, the PA test board transmits a multi-pulse excitation signal of three-cycle pulse train each with 500 ns pulsewidth in all of the following experiments [34].

B. Time-of-Flight A-Scan Measurements

First, we position the transducer directly above an agarose phantom as shown in Fig. 15(a). The distance between the agarose phantom and the transducer is varied from 17.5 to 40 mm in 2.5-mm increments using a vertical linear translation stage. For each measurement, the received TA signal from the transducer is amplified by an LNA, digitized by an oscilloscope, and repeated for 4000 averages. Fig. 15(b) shows the measured time-of-flight (ToF) in comparison to the expected ToF where the speed of sound (SoS) in mineral oil is 1440 m/s. The measured ToF matches closely with the expected ToF, corresponding to sub-mm errors in distance estimation.

In addition to ToF and distance measurements, we can also extract the thickness of the agarose block from the A-scan signal. Since TA signals are generated at interfaces with dielectric contrast that causes differential heating, signals from both the top and bottom edges of the agarose phantom can be delineated. In Fig. 15(c), we demonstrate this concept through A-scan measurements of two different agarose

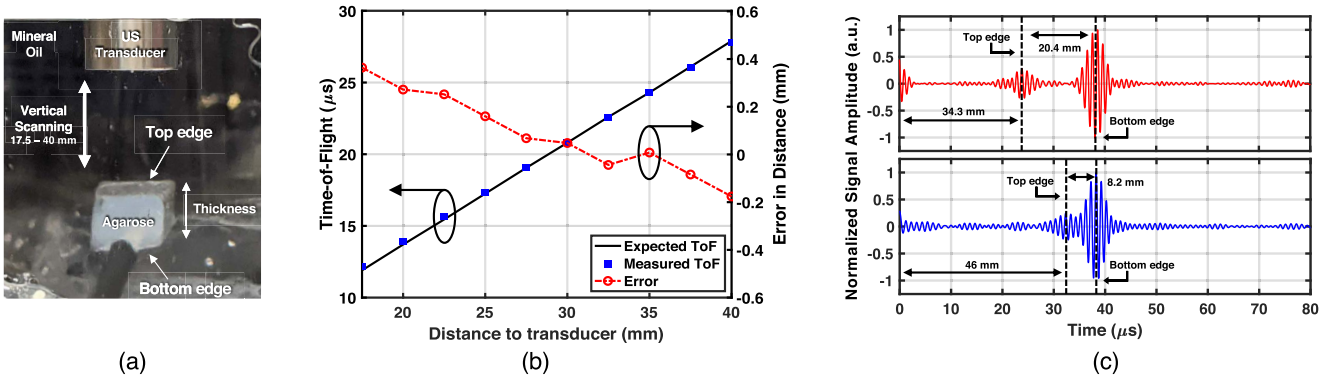

Fig. 15. (a) Experimental setup for A-scan measurements, (b) measured and expected ToF as a function of distance between the agarose phantom and the transducer, and (c) example A-scan measurement for a 19-mm-thick agar phantom that is 35 mm from the transducer (top) and for an 8-mm-thick agar phantom that is 45 mm from the transducer (bottom).

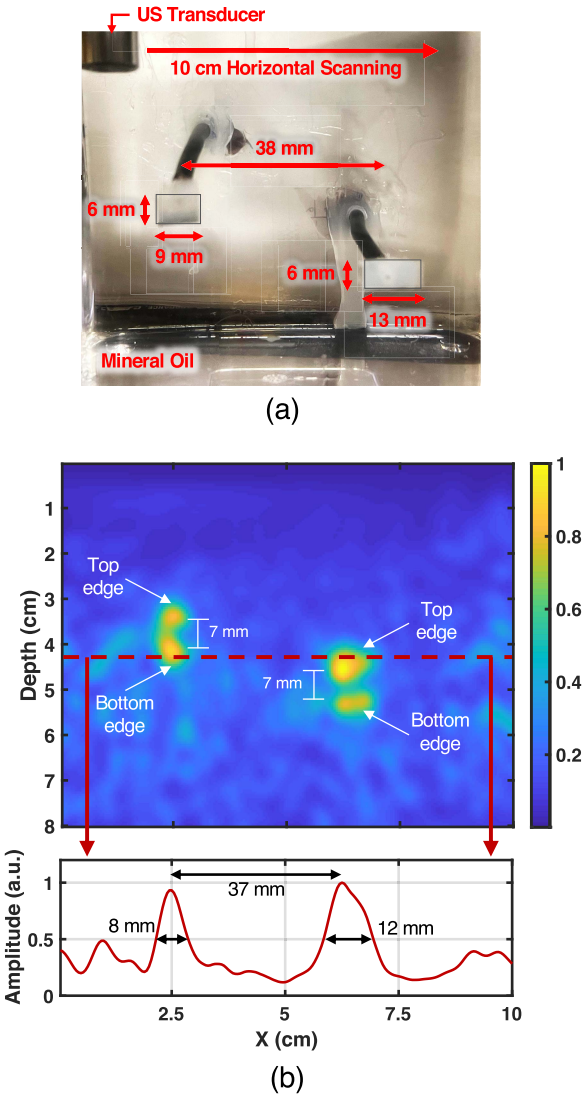

Fig. 16. (a) Experimental imaging setup with two agar phantoms and (b) reconstructed image from the TA measurements, with the cross section through the reconstructed image showing the two phantoms' relative location and sizes.

phantoms—one that is placed 35 mm from the transducer and is of 19 mm thickness and one that is placed 45 mm from the transducer and is of 8 mm thickness. As labeled in the figure, the thicknesses measured via the inter-echo time align closely with the ground truth.

C. Imaging Results

Although A-scan measurements provide distance information that can be deduced from the ToF, imaging offers spatial information that is required to understand the location and detailed structure of the target that is critical in real-world applications.

For the following TA imaging results, two agarose phantoms are submerged in the mineral oil as shown in Fig. 16(a). One agarose phantom is placed at a depth of approximately 3 cm and is 9 mm in length and the other is placed at a depth of approximately 4 cm and is 13 mm in length. To validate the multi-chip microwave excitation concept shown in Fig. 1, we use two PA ICs to independently source microwave power to the two phantoms. While direct coupling is employed here, it is important to note that future iterations could employ several PAs and remote antennas for microwave beamforming.

To enable imaging, we must scan the transducer—which is a single piezoelectric element—over an aperture. A horizontal linear translation stage is used to facilitate precise scanning and data capture over a 10-cm linear aperture in 1-mm increments. Following data capture, the signals are matched filtered for optimal noise reduction. Again, it is important to note that future iterations of the proposed system could exploit an electronically steerable, compact multi-element ultrasound transducer array and integrated front-end electronics [10]–[12].

A time-domain back-projection algorithm is employed to reconstruct the image displayed in Fig. 16(b) [35]. Similar to the A-scans, the top and bottom edges of the agarose phantoms can be distinctly noted. Likewise, the corresponding depths, sizes, and relative locations of the agarose blocks match closely with the ground truth. Reconstruction accuracy and resolution would further improve if a wider bandwidth ultrasound transducer was employed as the receiver.

VI. Conclusion

In this work, we present analysis of a detailed design methodology and measured results for a pulsed PA operating at multi-GHz frequencies with the highest demonstrated peak

power in PAs fabricated on a silicon substrate with deep submicron CMOS capability. A hybrid-stacked current-mode Class-D architecture using high-speed and high-voltage HBTs is used to achieve a high gain unit cell, with 2×2 DAT combining employed to achieve a multi-watt power output. Such a high-power design has unique challenges related to stability and device reliability. Current-starved inverter-based drivers were used to safeguard against device breakdown by controlling the rise time to prevent fast transients that lead to large voltage overshoots. We also determine optimal loading for the driving circuitry which mitigates the risk of oscillations by lowering the gain of any feedback loops that might cause instability. Electrical measurements of the PA demonstrate a 37.3-dBm peak P_{sat}, with 42% collector efficiency at 4.9 GHz while occupying a 4.87 mm^2 active area in 55-nm BiCMOS technology.

A compact, yet high-power microwave transmitter designed in a silicon process capable of deep submicron CMOS integration opens the door to a fully integrated and portable TA imaging system. Using the designed silicon PA presented in this work, we demonstrated end-to-end experimental TA sensing results. Results shown include precise TA distance measurements and multi-target localization via TA image reconstruction. The imaging results also incorporated the use of multiple PA ICs for microwave excitation of the targets. Future work aims to integrate several of the designed PA ICs in an array configuration such that beamforming techniques could be employed for targeted, application-specific, high SNR TA imaging that is not constrained by the peak power of a single chip.

ACKNOWLEDGMENT

The authors would like to thank STMicroelectronics for chip fabrication and Integrand Software for their EMX software.

REFERENCES

[1] P. Bonato, "Wearable sensors and systems," *IEEE Eng. Med. Biol. Mag.*, vol. 29, no. 3, pp. 25–36, May 2010.

[2] L. L. P. Wong, A. I. Chen, A. S. Logan, and J. T. W. Yeow, "An FPGA-based ultrasound imaging system using capacitive micromachined ultrasonic transducers," *IEEE Trans. Ultrason., Ferroelectr., Freq. Control*, vol. 59, no. 7, pp. 1513–1520, Jul. 2012.

[3] M. T. Ghasr, M. A. Abou-Khousa, S. Kharkovsky, R. Zoughi, and D. Pommerenke, "Portable real-time microwave camera at 24 GHz," *IEEE Trans. Antennas Propag.*, vol. 60, no. 2, pp. 1114–1125, Feb. 2012.

[4] J. A. Unar, W. C. Seng, and A. Abbasi, "A review of biometric technology along with trends and prospects," *Pattern Recognit.*, vol. 47, no. 8, pp. 2673–2688, Aug. 2014.

[5] M. S. Aliroteh and A. Arbabian, "Microwave-induced thermoacoustic imaging of subcutaneous vasculature with near-field RF excitation," *IEEE Trans. Microw. Theory Techn.*, vol. 66, no. 1, pp. 577–588, Jan. 2018.

[6] S. S. Ahmed, "Microwave imaging in security—Two decades of innovation," *IEEE J. Microw.*, vol. 1, no. 1, pp. 191–201, Jan. 2021.

[7] G. S. Kino, *Acoustic Waves: Devices, Imaging, and Analog Signal Processing (Prentice-Hall Signal Processing Series)*. Upper Saddle River, NJ, USA: Prentice-Hall, 1987.

[8] H. Nan, S. Liu, G. J. Buckmaster, and A. Arbabian, "Beamforming microwave-induced thermoacoustic imaging for screening applications," *IEEE Trans. Microw. Theory Techn.*, vol. 67, no. 1, pp. 464–474, Jan. 2019.

[9] C. Karunakaran, H. Zhao, H. Xin, and R. S. Witte, "Real-time volumetric thermoacoustic imaging and thermometry using a 1.5-D ultrasound array," *IEEE Trans. Ultrason., Ferroelectr., Freq. Control*, vol. 68, no. 4, pp. 1234–1244, Apr. 2021.

[10] K. Chen, H.-S. Lee, and C. G. Sodini, "A column-row-parallel ASIC architecture for 3-D portable medical ultrasonic imaging," *IEEE J. Solid-State Circuits*, vol. 51, no. 3, pp. 738–751, Mar. 2016.

[11] M. C. Chen *et al.*, "A pixel pitch-matched ultrasound receiver for 3-D photoacoustic imaging with integrated delta-sigma beamformer in 28-nm UTBB FD-SOI," *IEEE J. Solid-State Circuits*, vol. 52, no. 11, pp. 2843–2856, Nov. 2017.

[12] E. Kang *et al.*, "A variable-gain low-noise transimpedance amplifier for miniature ultrasound probes," *IEEE J. Solid-State Circuits*, vol. 55, no. 12, pp. 3157–3168, Dec. 2020.

[13] L. Huang, Z. Zheng, Z. Chi, and H. Jiang, "Compact thermoacoustic imaging system based on a low-cost and miniaturized microwave generator for *in vivo* biomedical imaging," *Med. Phys.*, vol. 48, no. 8, pp. 4242–4248, 2021.

[14] W. Simburger, H.-D. Wohlmuth, P. Weger, and A. Heinz, "A monolithic transformer coupled 5-W silicon power amplifier with 59% PAE at 0.9 GHz," *IEEE J. Solid-State Circuits*, vol. 34, no. 12, pp. 1881–1892, Dec. 1999.

[15] K. Datta and H. Hashemi, "2.9 A 29 dBm 18.5% peak PAE mm-Wave digital power amplifier with dynamic load modulation," in *IEEE ISSCC Dig. Tech. Papers*, Feb. 2015, pp. 1–3.

[16] H. T. Nguyen, D. Jung, and H. Wang, "4.9 A 60 GHz CMOS power amplifier with cascaded asymmetric distributed-active-transformer achieving watt-level peak output power with 20.8% PAE and supporting 2Gsym/s 64-QAM modulation," in *IEEE ISSCC Dig. Tech. Papers*, Feb. 2019, pp. 90–92.

[17] C. Sutardja, A. Cathelin, and A. Arbabian, "Portable thermoacoustic imaging for biometric authentication using a 37.3 dBm peak psat 4.9 GHz power amplifier in 55 nm BiCMOS," in *Proc. IEEE Radio Freq. Integr. Circuits Symp. (RFIC)*, Jun. 2021, pp. 7–10.

[18] X. Wang, D. R. Bauer, R. Witte, and H. Xin, "Microwave-induced thermoacoustic imaging model for potential breast cancer detection," *IEEE Trans. Biomed. Eng.*, vol. 59, no. 10, pp. 2782–2791, Oct. 2012.

[19] H. Nan and A. Arbabian, "Coherent frequency-domain microwave-induced thermoacoustic imaging," in *IEEE MTT-S Int. Microw. Symp. Dig.*, Jun. 2014, pp. 1–4.

[20] I. Aoki *et al.*, "A fully integrated quad-band GSM/GPRS CMOS power amplifier," in *IEEE ISSCC Dig. Tech. Papers*, Feb. 2008, pp. 570–636.

[21] M. Fathi, D. K. Su, and B. A. Wooley, "A 30.3 dBm 1.9 GHz-bandwidth 2×4-array stacked 5.3 GHz CMOS power amplifier," in *IEEE ISSCC Dig. Tech. Papers*, Feb. 2013, pp. 88–89.

[22] P. Chevalier *et al.*, "A 55 nm triple gate oxide 9 metal layers SiGe BiCMOS technology featuring 320 GHz f_T/370 GHz f_{MAX} HBT and high-Q millimeter-wave passives," in *IEDM Tech. Dig.*, Dec. 2014, p. 3.

[23] K. Datta and H. Hashemi, "Performance limits, design and implementation of mm-wave SiGe HBT class-E and stacked class-E power amplifiers," *IEEE J. Solid-State Circuits*, vol. 49, no. 10, pp. 2150–2171, Oct. 2014.

[24] K. Datta and H. Hashemi, "High-breakdown, high- f_{max} multiport stacked-transistor topologies for the W-band power amplifiers," *IEEE J. Solid-State Circuits*, vol. 52, no. 5, pp. 1305–1319, May 2017.

[25] T. S. D. Cheung and J. R. Long, "A 21-26-GHz SiGe bipolar power amplifier MMIC," *IEEE J. Solid-State Circuits*, vol. 40, no. 12, pp. 2583–2597, Dec. 2005.

[26] S. Cripps, *RF Power Amplifiers for Wireless Communications*, 2nd ed. Norwood, MA, USA: Artech House, 2006.

[27] D. Chowdhury, "Efficient transmitters for wireless communications in nanoscale CMOS technology," Ph.D. dissertation, EECS Dept., Univ. California, Berkeley, CA, USA, Dec. 2010. [Online]. Available: http://www2.eecs.berkeley.edu/Pubs/TechRpts/2010/EECS-2010-168.html

[28] J. Chen and A. M. Niknejad, "A compact 1 V 18.6 dBm 60 GHz power amplifier in 65 nm CMOS," in *Proc. IEEE Int. Solid-State Circuits Conf.*, Feb. 2011, pp. 432–433.

[29] M. Fathi, "Transformer array power combining and stacking for CMOS RF power amplifiers," Ph.D. dissertation, Stanford Univ., Stanford, CA, USA, Mar. 2013. [Online]. Available: https://searchworks.stanford.edu/view/9954589

[30] I. Ju, Y. Gong, and J. D. Cressler, "Highly linear high-power 802.11ac/ax WLAN SiGe HBT power amplifiers with a compact 2nd-harmonic-shorted four-way transformer and a thermally compensating dynamic bias circuit," *IEEE J. Solid-State Circuits*, vol. 55, no. 9, pp. 2356–2370, Sep. 2020.

[31] A. Serhan *et al.*, "A reconfigurable SOI CMOS Doherty power amplifier module for broadband LTE high-power user equipment applications," in *Proc. IEEE Radio Freq. Integr. Circuits Symp. (RFIC)*, Aug. 2020, pp. 79–82.

[32] H. Wang *et al.* (2000). *Power Amplifiers Performance Survey*. Accessed: Sep. 2021. [Online]. Available: https://gems.ece.gatech.edu/PA_survey.html

[33] A. T. Mobashsher and A. M. Abbosh, "Artificial human phantoms: Human proxy in testing microwave apparatuses that have electromagnetic interaction with the human body," *IEEE Microw. Mag.*, vol. 16, no. 6, pp. 42–62, Jul. 2015.

[34] A. Singhvi, A. Fitzpatrick, and A. Arbabian, "Resolution enhanced non-contact thermoacoustic imaging using coded pulse excitation," in *Proc. IEEE Int. Ultrason. Symp. (IUS)*, Sep. 2020, pp. 1–4.

[35] Y. Zhou, J. Yao, and L. V. Wang, "Tutorial on photoacoustic tomography," *J. Biomed. Opt.*, vol. 21, no. 6, Apr. 2016, Art. no. 061007.

Christopher Sutardja (Member, IEEE) received the Ph.D. degree in electrical engineering and computer sciences from the University of California, Berkeley, Berkeley, CA, USA, in 2017. His Ph.D. research focused on the design of wearable integrated radio frequency identification (RFID) readers for wireless power delivery/data communication with brain implants.

In 2018, he joined the Arabian Lab, Stanford University, Stanford, CA, USA, as a Post-Doctoral Scholar to work on integrated transmitters for portable microwave thermoacoustic imaging. His current research interests include integrated circuit design for imaging technologies, RF power amplifiers, wireless power delivery, and biomedical electronics.

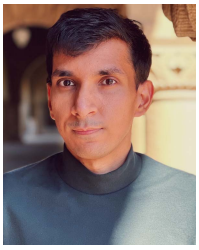

Ajay Singhvi (Graduate Student Member, IEEE) received the B.E. degree in electrical and electronics engineering from the Birla Institute of Technology and Science (BITS) Pilani, Pilani, India, in 2015. He is currently pursuing the M.S./Ph.D. degree in electrical engineering with Stanford University, Stanford, CA, USA.

From 2014 to 2015, he worked with Prof. Peter Beerel at the University of Southern California, Los Angeles, CA, USA, where his research was aimed at building low-power asynchronous circuits. In 2018, he was with Kilby Labs at Texas Instruments, Santa Clara, CA, USA, where he designed front-end architectures and circuits for LiDAR systems. He is currently with the Arbabian Lab, Stanford University, where his research is geared toward the development of multi-modal imaging systems for non-contact, airborne sensing of underground, underwater, and other complex environments by leveraging the unique advantages of both acoustics and electromagnetics. His research interests broadly lie in the design of integrated circuit systems, signal processing approaches, and algorithms for intelligent sensing and communication applications.

Mr. Singhvi was awarded the OPJEMS Scholarship in 2011, 2013, and 2014. He was a recipient of the L. K. Maheshwari Best Graduating Student Award from BITS Pilani in 2014 and the Analog Devices Outstanding Student Designer Award in 2020.

Aidan Fitzpatrick (Graduate Student Member, IEEE) received the B.S. degree in electrical and computer engineering from the University of Massachusetts Amherst, Amherst, MA, USA, in 2018, where he performed research on antenna design and RF system design, and the M.S. degree in electrical engineering from Stanford University, Stanford, CA, USA, in 2020, where he is currently pursuing the Ph.D. degree in electrical engineering.

His research interests are in computational imaging and perception systems—specifically at the intersection of electromagnetics, acoustics, and signal processing for the codesign of imaging algorithms and system hardware. His current projects focus on remote-sensing applications of non-contact thermoacoustic/photoacoustic imaging.

Andreia Cathelin (Senior Member, IEEE) started electrical engineering studies at the Polytechnic Institute of Bucarest, Romania, and graduated with M.S. degree from the Institut Supérieur d'Electronique du Nord (ISEN), Lille, France, in 1994. In 1998 and 2013 respectively, she received the Ph.D. and "habilitation 'a diriger des recherches" (French highest academic degree) from the Université de Lille 1, France.

Since 1998, she has been with STMicroelectronics, Crolles, France, now Technology RD Fellow. Her focus areas are in the design of RF/mmW/THz and ultra-low-power circuits and systems. She is the key design scientist in the promotion of all advanced CMOS technologies developed in the company. She is leading and driving research in advanced topics inside the company RD program and through leadership cooperation with major universities around the world. She has also management activities as being in charge of the ST-CMP operation (the CMP is an independent organization offering small series foundry services for SME and research institutes). She is very active in the IEEE community since more than 15 years, strongly implied with SSCS and its Adcom, the Executive Committee of VLSI Symposium and has been the TPC Chair of ESSCIRC 2020 and 2021 in Grenoble. She has been for ten years involved with ISSCC as RF subcommittee chair and then member of the Executive Committee. She is as well a Founding Member of the IEEE SSCS Women in Circuits Group. She has authored or coauthored more than 150 technical papers and 14 book chapters, has co-edited the book *The Fourth Terminal, Benefits of Body-Biasing Techniques for FDSOI Circuits and Systems* (Springer) and has filed more than 25 patents.

Dr. Cathelin was a co-recipient of the ISSCC 2012 Jan Van Vessem Award for Outstanding European Paper and of the ISSCC 2013 Jack Kilby Award for Outstanding Student Paper. She was the winner of the 2012 STMicroelectronics Technology Council Innovation Prize, for having introduced on the company's roadmap the integrated CMOS THz technology for imaging applications. Very recently, she has been awarded an Honorary Doctorate from the University of Lund, Sweden, promotion of 2020.

Amin Arbabian (Senior Member, IEEE) received the Ph.D. degree in electrical engineering and computer science from the University of California at Berkeley, Berkeley, CA, USA, in 2011.

From 2007 to 2008, he was a part of the Initial Engineering Team, Tagarray, Inc., Palo Alto, CA, USA (acquired by Maxim Integrated Inc.). In 2010, he joined Qualcomm's Corporate Research and Development Division, San Diego, CA, USA, where he designed circuits for next-generation ultra-low power wireless transceivers. In 2012, he joined Stanford University, Stanford, CA, USA, where he is currently an Associate Professor of electrical engineering. His current research interests include millimeter-wave and high-frequency circuits and systems, imaging technologies, Internet-of-Everything devices including wireless power delivery techniques, and medical implants.

Dr. Arbabian was a recipient or co-recipient of the 2010 IEEE Jack Kilby Award for Outstanding Student Paper at the International Solid-State Circuits Conference, and two-time second place best student paper awards at 2008 and 2011 RFIC Symposiums, the 2010–2011, 2014–2015, and 2016–2017 Qualcomm Innovation Fellowships, the 2013 IEEE International Conference on Ultra-Wideband, the 2013 Hellman Faculty Scholarship, the 2014 DARPA Young Faculty Award including the Director's Fellowship in 2016, the 2014 IEEE VLSI Circuits Symposium, the 2015 NSF CAREER Award, the 2016 Stanford University Tau Beta Pi Award for Excellence in Undergraduate Teaching, the 2016 IEEE Conference on Biomedical Wireless Technologies, Networks, and Sensing Systems, the Best Paper Awards at the 2017 IEEE Biomedical Circuits and Systems Conference, and the 2020 the IEEE TRANSACTIONS ON BIOMEDICAL CIRCUITS AND SYSTEMS Best Paper Award. He currently serves on the steering committee for RFIC Symposium, the technical program committees of RFIC Symposium and VLSI Circuits Symposium, and as an Associate Editor for the IEEE SOLID-STATE CIRCUITS LETTERS, and the IEEE JOURNAL OF ELECTROMAGNETICS, RF AND MICROWAVES IN MEDICINE AND BIOLOGY.